On the elasto-viscoplastic behavior of the Ti5553 alloy

Mohamed Ben Bettaieb [a,*], Thibaut Van Hoof [b], Thomas Pardoen [d], Philippe Dufour [d], Astrid Lenain [e], Pascal J. Jacques [d], Anne Marie Habraken [a,c]

[a] Department ArGEnCo, Division MS²F, University of Liège, Chemin des Chevreuils 1, 4000 Liège, Belgium
[b] CENAERO – Centre de Recherches en Aéronautique, Bâtiment Eole, Rue des Frères Wright, 29, B-6041 Gosselies, Belgium
[c] FNRS Fond National de la Recherche Scientifique, Belgium
[d] Institute of Mechanics, Materials and Civil Engineering, Université catholique de Louvain, B-1348 Louvain-la-Neuve, Belgium
[e] Techspace Aero, DT Matériaux & Procédés, Route de Liers 121, 04041 Milmort, Belgium

A B S T R A C T

The elastoviscoplastic behavior of the Ti5553 alloy is characterized and compared to the classical Ti–6Al–4V alloy. The true stress–strain curves are determined based on tensile tests performed under different strain rates at room temperature and at 150 °C, from which the elastic constants and the parameters of a Norton–Hoff viscoplastic model are identified. The strength of the Ti5553 alloy is 20–40% higher than the strength of the Ti–6Al–4V alloy. The Ti5553 alloy constitutes thus a promising candidate for advanced structural applications. In view of modeling structural applications of forming operations, the elastic and plastic initial anisotropy of the two alloys is investigated by combining compression on cylinders with elliptical sections, uniaxial tensile tests in different material directions, plane strain and shear tests. The initial anisotropy of the different alloys is very weak which justifies the modeling of the mechanical behavior with an isotropic yield surface. The identified elastoviscoplastic model is validated by comparing experimental results with FE predictions both on cylindrical notched specimens subjected to tensile tests and on flat specimens subjected to plane strain conditions.

1. Introduction

Titanium alloys are heavily used in aeronautic applications owing to a low density, good corrosion behavior, and excellent mechanical properties. The well-known Ti–6Al–4V is the most commonly selected Ti alloy in aerospace components. It accounts for more than 50% of the Ti production. However, the need to increase, for weight reduction reasons, the strength of Ti–6Al–4V components combined with the inherent limited strain hardening capacity has created an impetus for the development of new alloys. Over the past few years, Ti5553 has been identified as a promising candidate to advantageously replace Ti–6Al–4V in some components [1,2], but the mechanical data available for supporting such a choice are still scarce. Near β Ti5553 alloy (Ti–5Al–5V–5Mo–3Cr) [3] is a variation of the Russian alloy VT22 [4] and an alternative to the alloy Ti-10-2-3 [5].

The aim of the present work is to investigate the elastoviscoplastic mechanical response of the alloy Ti5553 under two heat treatment conditions (leading to two different microstructures named hereafter Ti5553-1 and Ti5553-3) involving a comparison with the Ti–6Al–4V alloy. The first objective of this paper is to identify the elastic constants and the Norton–Hoff viscoplastic parameters [6] based on uniaxial tensile tests carried out under four different strain rates ($5\times10^{-5}\,s^{-1}$, $2\times10^{-4}\,s^{-1}$, $4\times10^{-3}\,s^{-1}$, $10^{-2}\,s^{-1}$) and at two temperatures (room temperature and 150 °C). The second objective is to analyze the elastic and plastic anisotropy in view of modeling structural applications of forming operations. The anisotropy is investigated on the basis of compression tests, uniaxial tensile tests in different directions, plane strain tests and shear tests.

The outline of the work is the following:

- In Section 2, the chemical composition and heat treatment of the different microstructures are presented.
- In Section 3, the different mechanical parameters (elasticity, viscoplasticity) are identified after the presentation of the experimental procedure and results.
- In Section 4, the elastic and plastic anisotropy of the two alloys is analyzed.
- In Section 5, the identified elastoviscoplastic model is validated by comparing experimental results on notched and one plane strain specimens with FE predictions.
- In Section 6 the overall conclusions are highlighted.

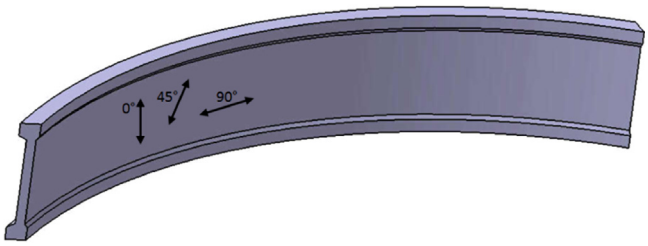

Fig. 1. Forged part made of alloy Ti–6Al–4V (with extraction directions).

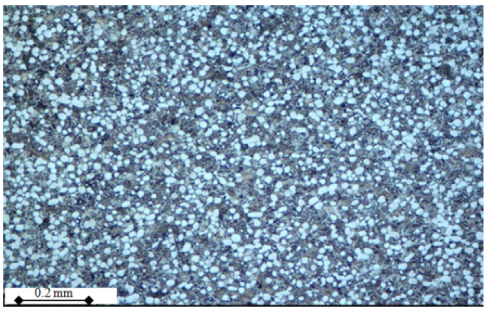

Fig. 2. Microstructure of alloy Ti–6Al–4V.

Table 1
Chemical composition of alloy Ti–6Al–4V, in weight per cent (wt%).

	C	Si	Mn	Mo	Al	V	Fe	Cu
Bottom	0.014	< 0.01	< 0.01	< 0.01	6.50	4.12	0.16	0.02
Top	0.012	< 0.01	< 0.01	< 0.01	6.46	4.05	0.15	0.03
	B	**Zr**	**Y**	**O**	**N**	**Sn**	**Cr**	**Ni**
Bottom	< 0.001	< 0.01	< 0.001	0.16	0.008	< 0.01	< 0.1	0.01
Top	< 0.001	< 0.001	< 0.001	0.18	0.006	< 0.01	0.1	0.01

Table 2
Chemical composition of the Ti5553 alloy (values are in wt%).

	Mo	Zr	Fe	V	Si	Al
Bottom	4.82	< 0.005	0.3	4.93	< 0.03	5.26
Top	4.87	< 0.005	0.3	4.94	< 0.03	5.33
	C	**O**	**N**	**Cr**	**Y**	**H**
Bottom	0.009	0.14	0.005	3.04	< 0.001	0.006
Top	0.007	0.14	0.004	3.05	< 0.001	0.004

2. Materials

As for any metallic alloys, the mechanical properties of Ti alloys are very sensitive to the initial microstructure, thermo-mechanical loading history, and chemical composition [7–10]. From a microstructural point of view, the Ti–6Al–4V and Ti5553 alloys are significantly different in terms of volume fraction and morphology of the primary α phase and of the transformed β phase. A detailed comparison between the microstructures of the two alloys can be found in [2].

2.1. Alloy Ti–6Al–4V

2.1.1. As received Ti–6Al–4V

The Ti–6Al–4V specimens are directly machined from a forged part provided by the company Techspace Aero (Fig. 1).

The Ti–6Al–4V alloy of this work is made of equiaxed primary α grains and secondary α lamellae dispersed in a β matrix (Fig. 2). The volume fraction of the α phase is between 80% and 90%. The transus temperature is about 995 °C [2,7]. After forging in several steps in the α+β domain, the final heat treatment consists in an annealing performed at 750 °C (1 h) followed by air cooling.

2.1.2. Chemical composition

The chemical composition from the top and bottom regions of the initial ingot (used to machine the forged component of Fig. 1) is reported in Table 1.

The molybdenum equivalent in terms of chemical composition is defined as follows [11]:

$$wt\%Mo.Eq. = 1.0\,(wt\%Mo) + 0.66\,(wt\%V) + 0.33\,(wt\%N) + 3\,(wt\%Fe) + 3\,(wt\%Cr). \quad (1)$$

Using the above table and formula, the Mo equivalent was estimated as equal to 3.48.

2.2. Ti5553 alloy

The Ti5553 alloy involves a large amount of β stabilizer elements such as Mo, V, Fe and Cr (see chemical composition in Table 2). The transus temperature is about 860 °C [4]. The Ti5553 alloy involves a high sensitivity to minute variations of the heat and thermomechanical treatment. This sensitivity has a significant impact on the microstructure as demonstrated hereafter.

The material of the present study has been provided by the company Techspace Aero in the form of forged pancakes (Fig. 3). The forging of the pancakes was performed at 815 °C using a 2500 tons forging press. The final thickness of the pancakes is equal to 47 mm. Based on the chemical composition (Table 2) and Eq. (1), the Mo equivalent was estimated as equal to 18.18.

The chemical composition from the top and bottom regions of the ingot is reported in Table 2.

The final heat treatment used to generate the two microstructures of Ti5553 alloy is defined by the following heat cycles (see Fig. 4):

- Ti5553-1: heated from room temperature up to 830 °C+hold at 830 °C during 2 h+air cooling+ageing at 610° C during 8 h+air cooling.
- Ti5553-3: heated from room temperature up to 830 °C+hold at 830 °C during 2 h+air cooling+ageing at 670° C during 8 h+air cooling.

The resulting microstructures are made of equiaxed primary α grains and secondary α needles embedded in a β matrix. These two microstructures are thus bi-modal; the primary α phase has a nodular morphology and the secondary α is lamellar. The volume fraction of the α phase is about 20%.

The first aging at 830 °C (Fig. 4) is responsible for the nucleation of the nodules of α. This aging is the same for both microstructures, explaining why there is no difference between the morphology and the size of the nodular α phase. The only difference between the two microstructures is related to the aging temperature. This temperature was responsible for the formation of the secondary α phase, which contains needles like particle shape or very small plates. The microstructure of Ti5553-1 shown in Fig. 5(a), is slightly finer compared to the Ti5553-3 microstructure shown in Fig. 5(b), due to a lower aging temperature (610 °C). Note that the presence of the secondary α phase is an important source of hardening in the alloy.

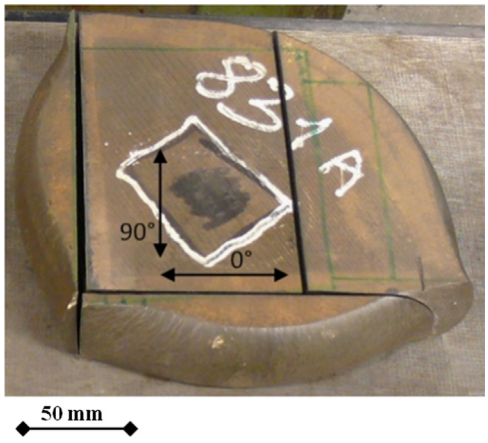

Fig. 3. Forged pancake of Ti5553 alloy.

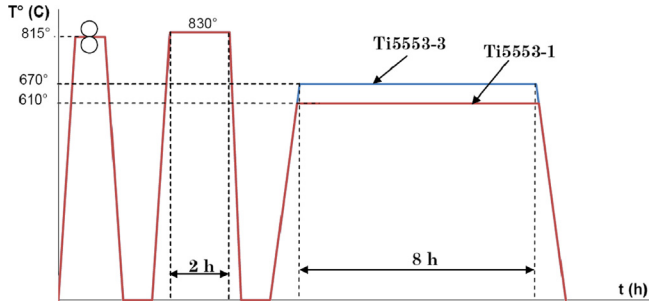

Fig. 4. Final heat treatment cycle of the two microstructures of the Ti5553 alloy.

3. Identification of the elastic and viscoplastic properties

This section is organized in the following way. The experimental procedures and test results are presented and discussed in Sections 3.1 and 3.2, respectively. The elastic and viscoplastic parameters are identified for the different alloys in the Section 3.3. The effect of some parameters on the elastoviscoplastic behavior is analyzed in the Section 3.4.

3.1. Mechanical test procedures

Uniaxial tensile tests were carried out on smooth axisymmetric specimens with a Zwick Z100 tensile machine equipped with a furnace and with the *Test Expert* software version 8.0. A load cell with a capacity of 100 kN was used. A tensile test performed at a constant crosshead velocity leads to a non-negligible decrease of the true strain rate during the test, which complicates the identification of the true mechanical behavior. In order to overcome this difficulty, a specific test software was programmed to adapt the crosshead speed during the test, ensuring constant strain rate inside the gauge length. These tests were performed at room temperature (RT) and at 150 °C. Different strain rates were used for the tests: $5\times10^{-5}\,s^{-1}$; $2\times10^{-4}\,s^{-1}$; $4\times10^{-3}\,s^{-1}$; $10^{-2}\,s^{-1}$. The tests were repeated three times for most temperature, strain rate and material/microstructure conditions, except when explicitly stated otherwise. The geometry and the dimensions of the specimens are defined in Fig. 6.

At RT, the displacement was measured by a longitudinal extensometer with a 50 mm gauge length. For some specimens, a transverse extensometer is also used in order to measure the radial displacement. At 150 °C, the tensile tests were performed in a temperature controlled chamber. The furnace, equipped with three independent heating zones, has a constant temperature zone of 80 cm. Thermocouples were used both in the chamber and directly on the specimen. The temperature was kept constant for about 30 min before testing to ensure homogeneous temperature in the grips and in specimen. The use of the furnace to carry out tensile tests at 150 °C limits the possibilities to measure specimen deformation during the test by an extensometer. The absence of a direct view inside the furnace eliminated the possibility to make use of an interferometry method or of a camera. Therefore, the deformation was determined from the displacement of the crosshead after careful correction for machine compliance.

3.2. Experimental results

The present section addresses the elastic and viscoplastic (pre- and post-necking) domains. Focus is placed on the experimental repeatability, on the effect of the strain rate and temperature, and on the differences between the different alloys and microstructures. First, the results are discussed in terms of the engineering stress (σ_{eng})–strain (ε_{eng}) curves defined by the following relationships:

$$\sigma_{eng}=\frac{F}{S_0};\quad \varepsilon_{eng}=\frac{u}{l_0}, \tag{2}$$

where F is the tensile force; S_0 is the initial cross section area of the specimen; l_0 is the initial gauge length (equal to 40 or 50 mm); u is the longitudinal displacement measured by the extensometer.

The correction for machine compliance is used in order to compute the strain ε_{eng} at 150 °C from the grip displacements.

3.2.1. Dispersion in the mechanical response

Table 3 provides the value of σ_0 and R_m which refer to the stress corresponding to the onset of plasticity and to the maximum nominal stress respectively (three values per case). Dev(x) defines the deviation on the quantity x, i.e. the ratio between Δx and x_{mean} with Δx the difference between the largest and the smallest value of x and x_{mean} the average of the three values of x. This table shows that the deviation on σ_0 and R_m does not exceed 3.2%.

3.2.2. Effect of strain rate

Fig. 7 shows the effect of the strain rate on the engineering stress–strain curves. In order to accurately analyze this effect, a zoom on the stress domain (900–1600 MPa) for the Ti5553 microstructures and (700–1200 MPa) for the Ti–6Al–4V alloy is considered. For the sake of clarity, only the intermediate curve from the three duplicate tests is plotted. The different alloys involve a clear influence of the strain rate in the nonlinear regime. The tensile stress generally increases with increasing strain rates. The elastic behavior remains insensitive to strain rate.

3.2.3. Effect of temperature

The engineering stress–strain curves presented in Fig. 8 show that the plastic flow is affected not only by the strain rate, but also by the temperature. The temperature affects both the linear and the nonlinear behavior. Here, the effect of temperature on the force–displacement response is analyzed for the Ti5553-1 microstructure and for two strain rates ($10^{-2}\,s^{-1}$ and $4.\,10^{-3}\,s^{-1}$), but the effect is common to the different alloys. The linear elastic response exhibits a decrease of the Young's modulus when the temperature increases (Section 3.3.1 for the exact Young's modulus value). In the nonlinear regime, the maximum stress decreases with increasing temperature. A higher temperature reduces the thermally activated part of the resistance to dislocation movements and results in higher dislocation mobility.

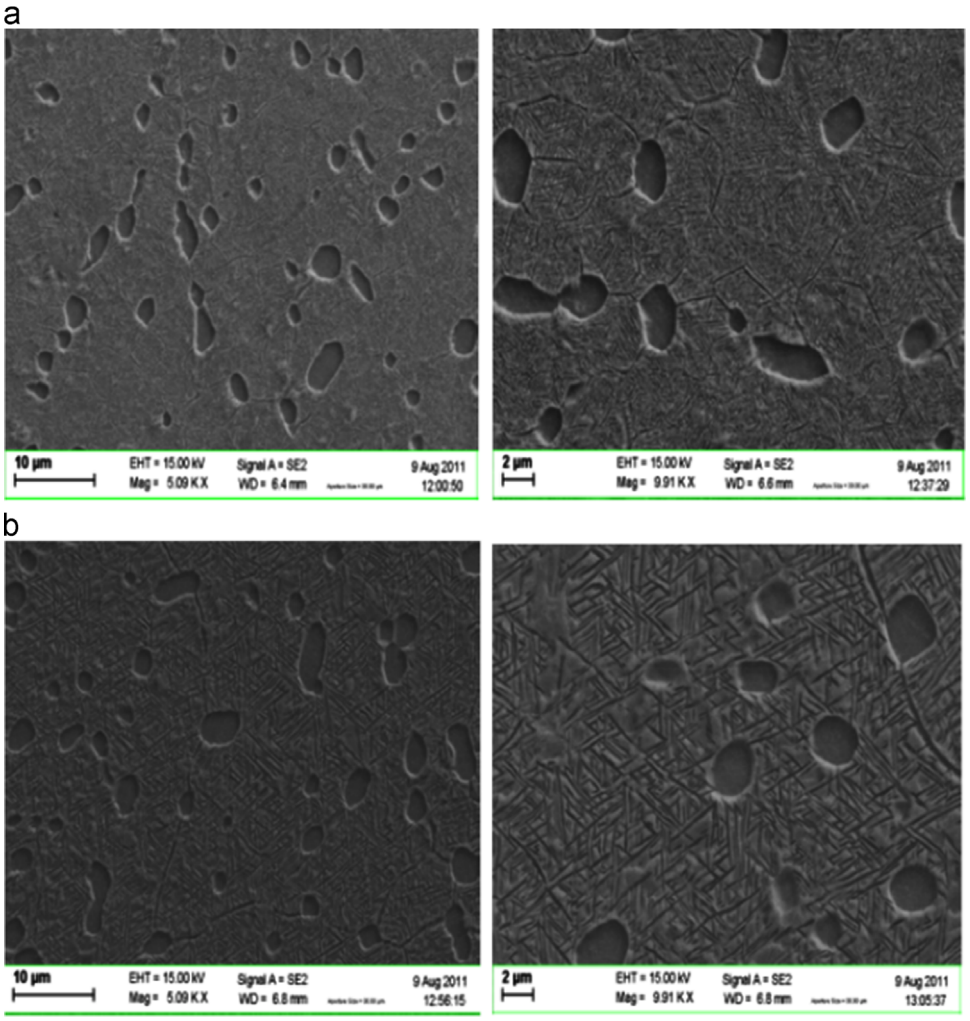

Fig. 5. Scanning electron microscopy micrographs of two Ti5553 heat treatment conditions: (a) Ti5553-1 (aging at 610 °C) and (b) Ti5553-3 (aging at 670 °C).

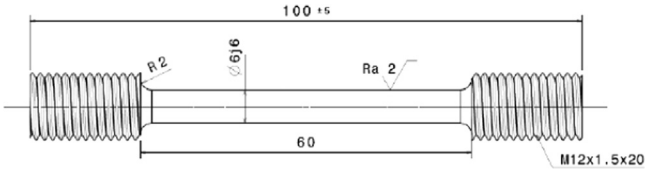

Fig. 6. Uniaxial tensile test geometry and dimensions.

3.2.4. Comparison between the mechanical response of the different microstructures

Fig. 9 compares the engineering stress–strain curves of the different alloys at two different temperatures. Here, the three tests per alloy are plotted. In the linear domain, the Young's modulus of the Ti5553 is smaller than the Young's modulus of the Ti–6Al–4V (see Table 4 for the exact values of the Young's modulus). The tensile strength is higher for the Ti5553 compared to the Ti–6Al–4V. This higher strength justifies the interest for the Ti5553 as a promising candidate for advanced structural applications when compared to the traditional Ti–6Al–4V alloy, which is consistent with earlier studies [1,2].

3.3. Identification of the material parameters

The displacement u is used to compute the true strain and the true stress as

$$\varepsilon = ln\left(\frac{l_0+u}{l_0}\right); \quad \sigma = \frac{F}{S} = \frac{F}{S_0 e^{-\varepsilon}}. \tag{3}$$

These formulae are valid only for uniform stress and strain distribution across the section of the specimen, i.e., before the onset of necking.

3.3.1. Elastic parameters

Contrarily to several works ([12] among others), the elastic behavior of the Ti alloys investigated here is assumed isotropic. This assumption will be assessed in Section 4. The Young's modulus and the Poisson ratio are determined from uniaxial tensile tests. The elastic properties were determined within the first 80% of the initial linear region of the stress–strain curve. The values of the Young's modulus of the different alloys and microstructures are given in Table 4. These values are measured as the average over 12 specimens for each microstructure and alloy.

In order to identify the Poisson ratio, a radial extensometer was used. This ratio is assumed to be independent of the strain rate and the temperature and it is found to be close to 0.33 ± 0.03 for the different alloys and microstructures.

A compilation of the Young's modulus and Poisson ratio found at RT for different Ti–6Al–4V alloys from the literature is given in Table 5, consistent with our measurements.

3.3.2. Evolution of yield stress and ultimate tensile stress

Tables 6 and 7 summarize the average values and standard deviation of the conventional yield stress defined at 0.2% of plastic strain $\sigma_{p\ 0.2}$ and of the ultimate stress σ_u (expressed in MPa) for the

Table 3
Magnitude and dispersion on the stress at the onset of plasticity and on the maximum tensile stress.

Micro; $\dot{\varepsilon}$; temperature	σ_0 (MPa)	Dev (σ_0) (%)	R_m (MPa)	Dev (R_m) (%)
Ti5553-1; $10^{-2}\,s^{-1}$; RT	1337; 1347; 1354	1.2	1363; 1393; 1364	2.1
Ti5553-1; $10^{-2}\,s^{-1}$; 150 °C	1171; 1174; 1180	0.75	1245; 1243; 1218	2.15
Ti5553-3; $10^{-2}\,s^{-1}$; RT	1164; 1202; 1179	3.15	1208; 1193; 1225	2.6
Ti–6Al–4V; $10^{-2}\,s^{-1}$; 150 °C	970; 991; 987	2.15	1003; 999; 1000	0.4

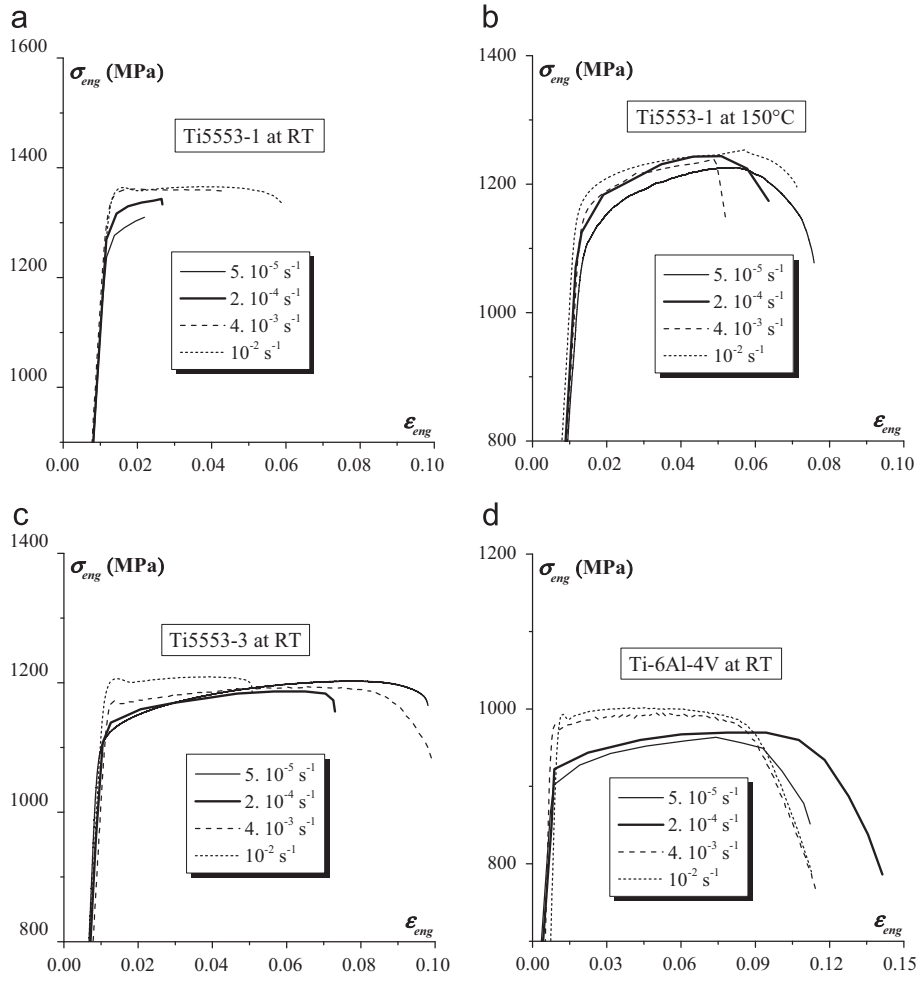

Fig. 7. Effect of the strain rate on the engineering stress–strain curve (the axes are not plotted with the same scale): (a) Ti5553-1 at RT, (b) Ti5553-1 at 150 °C, (c) Ti5553-3 at RT, and (d) Ti–6Al–4V at RT.

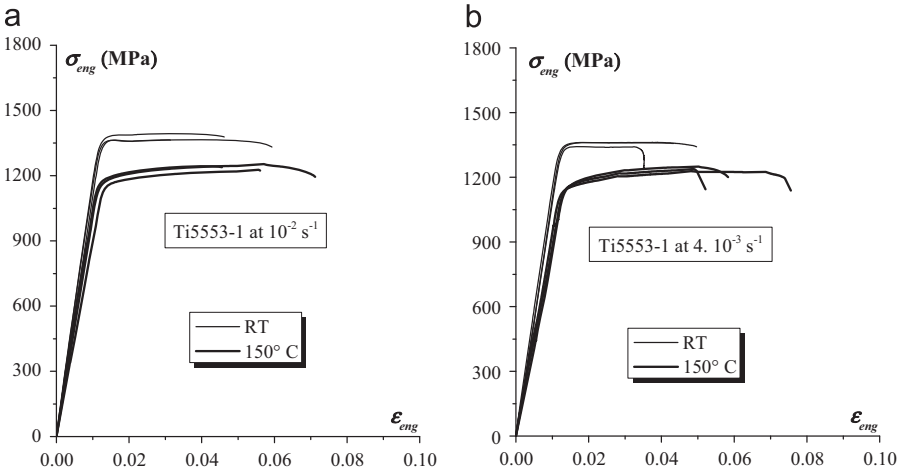

Fig. 8. Effect of the temperature on the engineering stress–strain curve: (a) Ti5553-1 at $10^{-2}\,s^{-1}$; (b) Ti5553-1 at $4 \times 10^{-3}\,s^{-1}$.

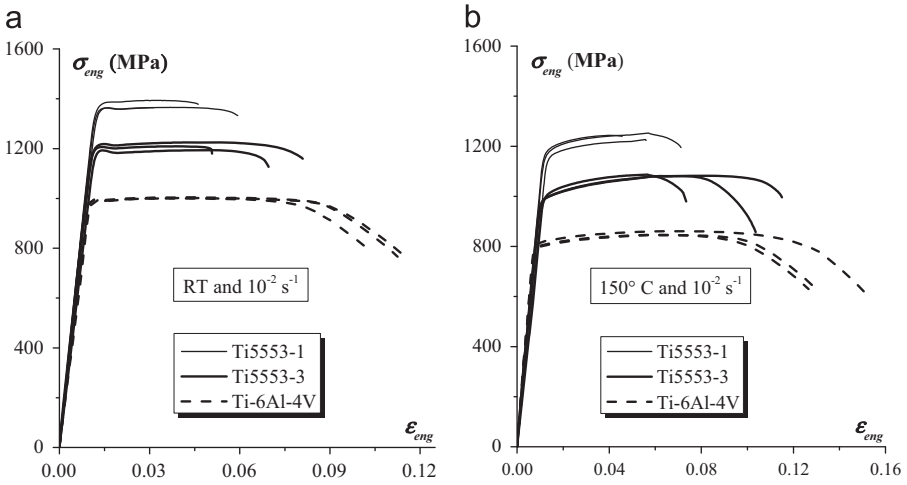

Fig. 9. Comparisons between the engineering stress–strain curves of the different alloys: (a) Tests performed at RT and 10^{-2} s^{-1}, (b) Tests performed at 150 °C and 10^{-2} s^{-1}.

Table 4
Young's modulus of Ti–6Al–4V and Ti5553 alloys.

Alloy	RT	150 °C
Ti5553-1	113 ± 7 GPa	89 ± 5 GPa
Ti5553-3	107 ± 8 GPa	86 ± 6 GPa
Ti–6Al–4V	118 ± 12 GPa	94 ± 10 GPa

Table 5
Values of the Young's modulus and Poisson ratio of Ti–6Al–4V at room temperature from the literature.

Ref.	[14]	[15]	[16]	[17]	[18]	[8]
E **(GPa)**	102	117	108	112	107–122	112–114
Ref.	[14]	[19]	[20]	[21]	[8]	[22]
ν	0.34	0.33	0.34	0.34	0.26–0.36	0.34

different strain rates and temperatures, respectively. Both strength indicators increase with increasing strain rate and decrease with increasing temperature, as expected.

3.3.3. Viscoplastic model

A hardening law, frequently used for Ti alloys [12,22], is the one proposed by Norton [23,24] and generalized to 3D by Hoff:

$$\overline{\sigma} = exp(-P_1\overline{\varepsilon})\sqrt{3}P_2(\sqrt{3}\dot{\overline{\varepsilon}})^{P_3}\overline{\varepsilon}^{P_4}, \tag{4}$$

where $\overline{\sigma}$, $\overline{\varepsilon}$ and $\dot{\overline{\varepsilon}}$ are the Von Mises equivalent stress, equivalent strain and equivalent strain rate, respectively:

$$\overline{\sigma} = \sqrt{\frac{3}{2}\hat{\sigma}_{ij}\hat{\sigma}_{ij}}; \quad \dot{\overline{\varepsilon}} = \sqrt{\frac{2}{3}\dot{\hat{\varepsilon}}_{ij}\dot{\hat{\varepsilon}}_{ij}}; \quad \overline{\varepsilon} = \int_0^t \dot{\overline{\varepsilon}}\, dt; \tag{5}$$

where $\hat{\sigma}_{ij}$ are the deviatoric components of the stress tensor; $\dot{\hat{\varepsilon}}_{ij}$ are the deviatoric components of the strain rate tensor; P_1 is a softening parameter; P_2 is a scaling factor; P_3 is the strain rate sensitivity exponent; P_4 is the hardening exponent.

The J_2 viscoplastic theory is based on the following set of equations [12]

$$\dot{\hat{\varepsilon}}_{ij} = \frac{3\dot{\overline{\varepsilon}}}{2\overline{\sigma}}\hat{\sigma}_{ij} \tag{6}$$

Hence, the relationship between the deviatoric stress, $\hat{\sigma}_{ij}$, and the deviatoric strain rate, $\dot{\hat{\varepsilon}}_{ij}$, tensors writes for a Norton–Hoff hardening law:

$$\hat{\sigma}_{ij} = 2P_2(\sqrt{3}\dot{\overline{\varepsilon}})^{P_3-1}(\overline{\varepsilon})^{P_4}exp(-P_1\overline{\varepsilon})\dot{\hat{\varepsilon}}_{ij}. \tag{7}$$

The use of an isotropic model is justified in Section 4.

Table 6
Effect of the strain rate and temperature on the initial yield stress $\sigma_{p\ 0.2}$ (MPa).

$\dot{\varepsilon}$ **(s^{-1})**	$\sigma_{p\ 0.2}$ **of Ti5553-1**		$\sigma_{p\ 0.2}$ **of Ti5553-3**		$\sigma_{p\ 0.2}$ **of Ti–6Al-4V**	
	RT	150 °C	RT	150 °C	RT	150 °C
$\mathbf{5\times10^{-5}}$	1290 ± 10	1157 ± 28	1123 ± 15	1001 ± 20	912 ± 5	738 ± 3
$\mathbf{2\times10^{-4}}$	1336 ± 10	1158 ± 8	1144 ± 6	1007 ± 17	934 ± 7	766 ± 10
$\mathbf{4\times10^{-3}}$	1362 ± 9	1187 ± 8	1187 ± 18	1027 ± 8	988 ± 17	806 ± 20
$\mathbf{10^{-2}}$	1382 ± 9	1198 ± 8	1218 ± 12	1035 ± 13	995 ± 2	817 ± 9

Table 7
Effect of the strain rate and temperature on the ultimate stress σ_u (MPa).

$\dot{\varepsilon}$ **(s^{-1})**	σ_u **of Ti5553-1**		σ_u **of Ti5553-3**		σ_u **of Ti–6Al–4 V**	
	RT	150 °C	RT	150 °C	RT	150 °C
$\mathbf{5\times10^{-5}}$	1375 ± 14	1303 ± 20	1260 ± 30	1172 ± 25	1046 ± 3	880 ± 2
$\mathbf{2\times10^{-4}}$	1390 ± 24	1300 ± 17	1268 ± 46	1179 ± 5	1062 ± 10	872 ± 35
$\mathbf{4\times10^{-3}}$	1404 ± 15	1314 ± 8	1278 ± 25	1183 ± 5	1044 ± 13	911 ± 15
$\mathbf{10^{-2}}$	1430 ± 23	1312 ± 17	1272 ± 20	1176 ± 13	1060 ± 6	921 ± 14

The material parameters (P_1, P_2, P_3 and P_4) are adjusted to fit the Norton–Hoff law to the experimental curves. A fitness scalar (noted hereafter R) is defined to describe the 'distance' between the experimental results $\overline{\sigma}_S^{Exp}(\dot{\overline{\varepsilon}}, \overline{\varepsilon})$ (where s refers to the number of the duplicate tensile test ranging between 1 and 3) and the Norton–Hoff equation $\overline{\sigma}^{NH}(\dot{\overline{\varepsilon}}, \overline{\varepsilon})$ as evaluated with a given set of parameter values. The experimental curves and the Norton–Hoff curve are sampled at different strain positions (200 points) which are used to evaluate R as follows:

$$R(\overline{\sigma}) = \sum_{S=1}^{3}\sum_{\dot{\overline{\varepsilon}}^p}\sum_{\overline{\varepsilon}^p}(\overline{\sigma}_S^{Exp}(\dot{\overline{\varepsilon}}, \overline{\varepsilon}) - \overline{\sigma}^{NH}(\dot{\overline{\varepsilon}}, \overline{\varepsilon}))^2. \tag{8}$$

The optimal set of material parameters (P_1, P_2, P_3 and P_4) is obtained by a minimization of the fitness scalar R. This minimization was performed with a homemade python script based on the Nelder–Mead Simplex algorithm. For more details about this algorithm, see [26].

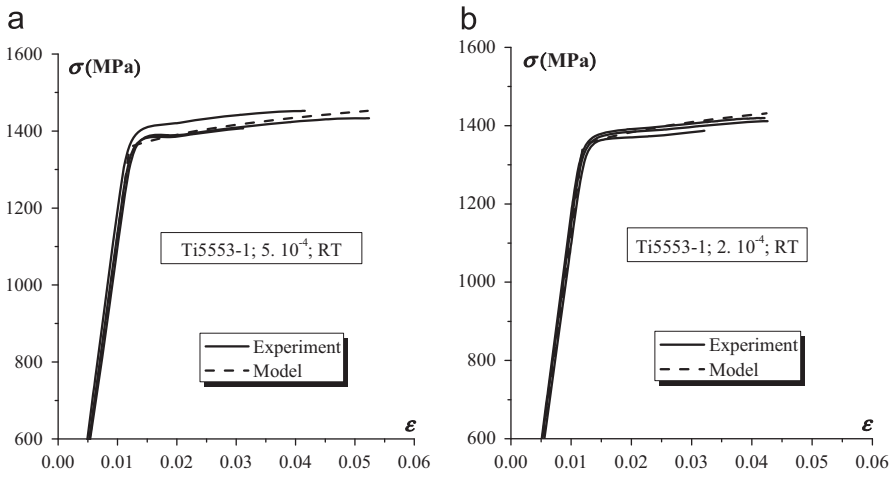

Fig. 10. Results of the identification of the flow properties and assessment with respect to the experimental data.

Table 8
Parameters of the Norton–Hoff law.

	RT				150°			
	P_1	P_2	P_3	P_4	P_1	P_2	P_3	P_4
Ti5553-1	0.00187	982	0.006	0.045	0.0028	964	0.0015	0.077
Ti5553-3	0.005	872	0.0035	0.05	0.0018	860	4.8×10^{-05}	0.0874
Ti–6Al–4V	5.2×10^{-05}	758	0.0097	0.051	0.004	678	0.013	0.072

Eq. (4) is supplemented by the following elastic relationship describing the mechanical response in the elastic domain:

$$\sigma = E\,\varepsilon^{el}, \tag{9}$$

where E is the Young's modulus and ε^{el} is the elastic strain in the tensile direction.

The full model is then composed by Eq. (9) for elastic strain and of Norton–Hoff's law (4) for the viscoplastic behavior. The transition strain from elastic to viscoplastic behavior is identified by the intersection between the linear elastic and Norton–Hoff response.

Fig. 10 illustrates the result of the identification procedure.

All viscoplastic parameters determined from the identification procedure at RT and 150 °C are given in Table 8. The effect of the strain rate on the stress–strain curve of Ti5553-3 material at 150 °C is relatively minor as indicated by the small value of the parameter P_3 (Table 8).

3.4. Analysis of the effect of the mechanical, chemical and microstructural parameters on the elastoviscoplastic behavior

The Young's modulus decreases with increasing temperature, as expected. Regarding plasticity, the movement of dislocations is easier with increasing temperature owing to the operation of thermally activated mechanisms which reduce hardening. Table 9 shows the ratio of the $\sigma_{p\ 0.2}$ at 150 °C and at RT, as well as for σ_u, from which we conclude that the mechanical behavior of Ti–6Al–4V alloy is more sensitive to temperature than Ti5553 alloy. Note also that the strain hardening exponent P_4 increases with temperature. In terms of the Considère criterion, an increase of strain hardening capacity reflects in an increase of the uniform elongation. Here, there is no significant difference between Ti5553 and Ti–6Al–4V alloys.

Except if it induces a large temperature increase, an increase of strain rate generally generates higher resistance to plastic flow [27], as confirmed for the three studied materials on the initial yield stress $\sigma_{p\ 0.2}$ and ultimate stress σ_u. The strain rate effect is here moderate, which is consistent with the literature (see for instance Refs. [28,29]).

Table 9
Effect of the temperature on $\sigma_{p\ 0.2}$ and σ_u.

	Ti5553-1	Ti5553-3	Ti–6Al–4V
$\sigma_{p\ 0.2}$ ***(150 °C)/$\sigma_{p\ 0.2}$ (RT)***	0.86–0.9	0.85–0.89	0.8–0.82
σ_u ***(150 °C)/σ_u (RT)***	0.91–0.94	0.92–0.93	0.82–0.87

The Mo equivalent (see Sections 2.1.1 and 2.2) has been empirically related to the yield stress [2,30]. The Ti555 alloy (two microstructures) has an Mo-equivalent nearly 5 times higher than in the Ti–6Al–4V alloy, in agreement with the larger strength.

The effect of the size of the secondary α particles on strength ($\sigma_{p\ 0.2}$ and σ_u) can be explained by an Hall–Petch type effect [27,31]. The Hall–Petch model states that the yield stress is inversely proportional to the square root of the grain size. Physically, the phase boundaries between the β phase and the secondary α precipitates act as barriers to dislocations motion. As the size of the secondary α precipitates is smaller and their number is higher in the Ti5553-1 microstructure compared to the Ti5553-3, it involves more barriers. So the stress required to multiply dislocations and propagate plastic flow is larger for Ti5553-1 microstructure. Similar observation has been made for instance in DP steels with different sizes of the ferrite grains surrounded by hard martensite grains [32].

4. Study of the elastic and plastic anisotropy

In the previous sections, the behavior of the Ti–6Al–4V and of the two microstructures of Ti5553 was assumed to be elastically and plastically isotropic. The purpose of this section is to check the validity of this assumption using different mechanical tests (see

Table 10). Three specimens or more are tested for each mechanical test. The anisotropy directions are defined in Figs. 1 and 3 for the Ti–6Al–4V and Ti5553 alloys, respectively.

4.1. Mechanical tests

4.1.1. Uniaxial tensile test at 0°, 45° and 90°

The orientation of the specimens used for evaluating the anisotropy is defined in Fig. 1. The 0° direction coincides with the axis of the sector of the circular forged component part, and the 90° direction with the tangential direction.

4.1.2. Plane strain tests

The plane strain tests were performed with a bi-axial test machine developed within the ArGenCo department of the University of Liege, based on the design proposed by Pijlman [33]. This machine is equipped with a 100 kN load cell. The geometry of the plane strain specimens is shown in Fig. 11(a). The thickness of the specimen is uniform and equal to 1 mm. In order to ensure that cracking occurs first at the center of the gauge section and to minimize the edge effects, a notch with a 1.5 mm radius was machined in the central region of the specimen. This specimen shape was already tested in earlier studies [34–38] for applications on steel grades. The specimens are tested at a velocity of 0.3 mm/min.

4.1.3. Shear tests

Shear tests were performed with the same machine as the plane strain tests. The geometry of the specimen is shown in Fig. 11(b). This specimen was tested at 0.3 mm/min displacement rate. To ensure that cracking occurs first at the center of the gauge section, the central region has a smaller thickness of 1.5 mm, much smaller than the thickness of the shoulder region equal to 7.0 mm. The specimens were cut in such a way that the shear direction coincides with the 0° direction (see Fig. 1) for the Ti–6Al–4V specimens.

4.1.4. Compression tests

The compression tests were performed using a SCHENCK Hydropuls 400 kN machine. In order to further investigate the anisotropy effects, the section of the compression specimen was chosen as elliptic. The geometry and the dimensions of the specimen are given in Fig. 11(c). The specimens used for the compression tests on the Ti5553 microstructures were cut with the compression axis along the 0° direction (see Fig. 3). For the case of Ti–6Al–4V material, the compression specimens were cut in three different directions: in the axial, radial and tangential directions of the forged part (see Fig. 1).

Table 10
Tests performed to investigate the mechanical anisotropy.

Loading state	Ti5553 alloy	Ti–6Al–4V
Uniaxial tensile (UT) in 0°, 45° and 90°		X
Plane strain (PS) in 0°	X	X
Shear (*S*) in 0°	X	X
Compression (*C*) in 0°	X	X

4.2. Elastic anisotropy

The elastic anisotropy of the different materials is investigated on the basis of the slope of the elastic part of the stress–strain curves corresponding to the different tests S_{UT}, S_{PS}, S_S and S_C are the elastic slopes corresponding to uniaxial tensile, plane strain, shear and compression, respectively. In the case of elastic isotropy, these slopes are related to the Young's modulus E and Poisson ratio ν by the following relationships:

$$S_{UT} = E; \quad S_{PS} = \frac{E}{1-\nu^2}; \quad S_S = \frac{E}{1+\nu}; \quad S_C = E. \tag{10}$$

Table 11 gathers the values of the measured slopes. The theoretical isotropic values (noted "*Theo*" and expressed in GPa) of the different slopes are computed on the basis of Eq. (10), where the Young's modulus value is taken from the uniaxial tensile state (see Table 4) and the Poisson ratio ν is assumed to be equal to 0.33 as mentioned in Section 3.3.1. One can check that the theoretical isotropic slopes are close to the experimental ones for the different stress states. The elastic behavior of the different alloys and microstructures can thus be considered as isotropic.

4.3. Plastic anisotropy

The experimental characteristic points of the yield locus are recorded for each material in order to determine the degree of the

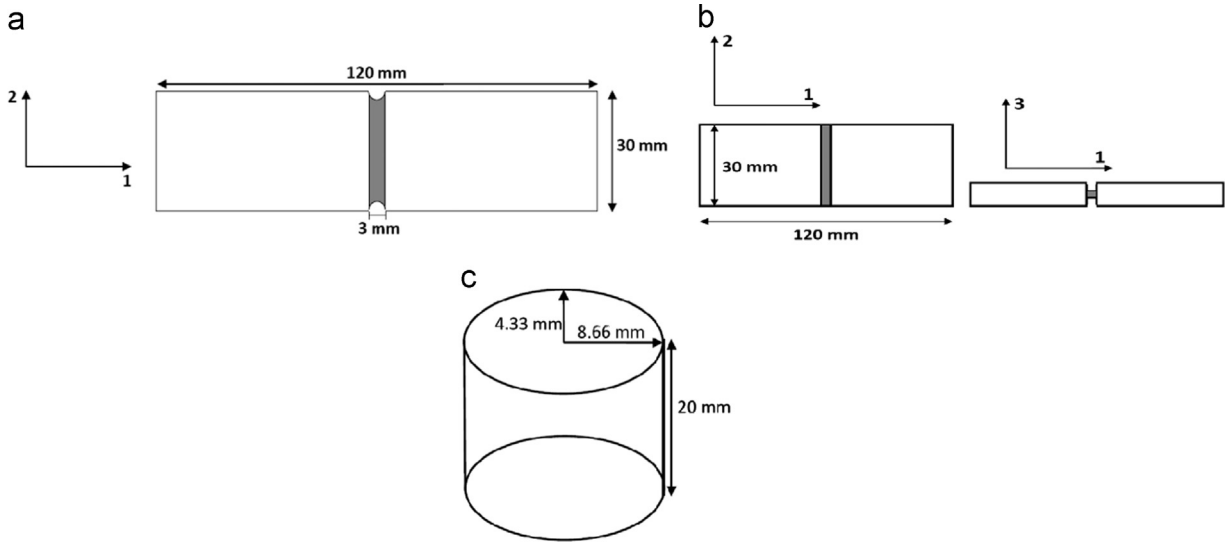

Fig. 11. Geometry and dimensions of the specimens used for evaluating the degree of anisotropy: (a) plane strain tests, (b) shear test, and (c) compression tests.

initial plastic anisotropy of the different alloys. The yield stress must be determined for the different stress states. However, as shown in Table 6, the strength is sensitive to the strain rate and the strain rates vary among the different tests. In order to eliminate the viscosity effect, the yield stresses are estimated at the same or almost similar equivalent strain rate (a numerical procedure is developed and used for this purpose).

Fig. 12 shows that the experimental points are located between the Tresca and Von Mises yield loci. This result implies that the initial plastic anisotropy is very low. This conclusion justifies the assumption of initial plastic isotropy for modeling the deformation of the different materials used in Section 5. The experimental yield locus shows a slight asymmetry: the yield stress in uniaxial compression is higher than the yield stress in uniaxial tension. This observation confirms earlier results announced in the literature [39–42]. Numerical simulations are provided in Section 5 in order to model the plane strain test and to further check the validity of the isotropy assumption.

Table 11
Elastic stiffness measured under different loading conditions, slope values in GPa.

	Plane strain (S_{PS} in GPa)		Shear (S_S in GPa)		Compression (S_C in GPa)	
	Exp	**Theo**	**Exp**	**Theo**	**Exp**	**Theo**
Ti5553-1	125 ± 9	128 ± 8	75 ± 4	84 ± 5	117 ± 2	113 ± 7
Ti5553-3	123 ± 7	122 ± 10	74 ± 4	79 ± 6	113 ± 2	107 ± 8
Ti–6Al–4V	115 ± 2	134 ± 15	74 ± 7	87 ± 9	126 ± 7	118 ± 12

5. Validation of the elastoviscoplastic constitutive law by FE simulations

The identified constitutive elastoviscoplastic model has been validated by comparing, at the global and local levels, numerical simulations and experimental tests on notched and plane strain specimens not used for the identification process.

5.1. Validation of the elastoviscoplastic parameters

Numerical simulations of three cylindrical notched round specimens (R_0=1, 2 and 4 mm) under tensile loading were performed using the Lagamine finite element code, developed at the University of Liège [43]. The elastoviscoplastic parameters of the Ti5553-1 microstructure are used in these simulations with axisymmetric conditions. The geometrical details of the simulated specimens are given in Fig. 13, while the finite element meshes are shown in Fig. 14. The symmetry of the problem allows the modeling of one half of the specimen only. The loading is applied through the prescribed displacement rate equal to 1 mm/min at the upper edge of the specimen. A refined mesh is generated near the notch where large strain gradients are expected, whereas a coarser discretization is used in the rest of the specimen.

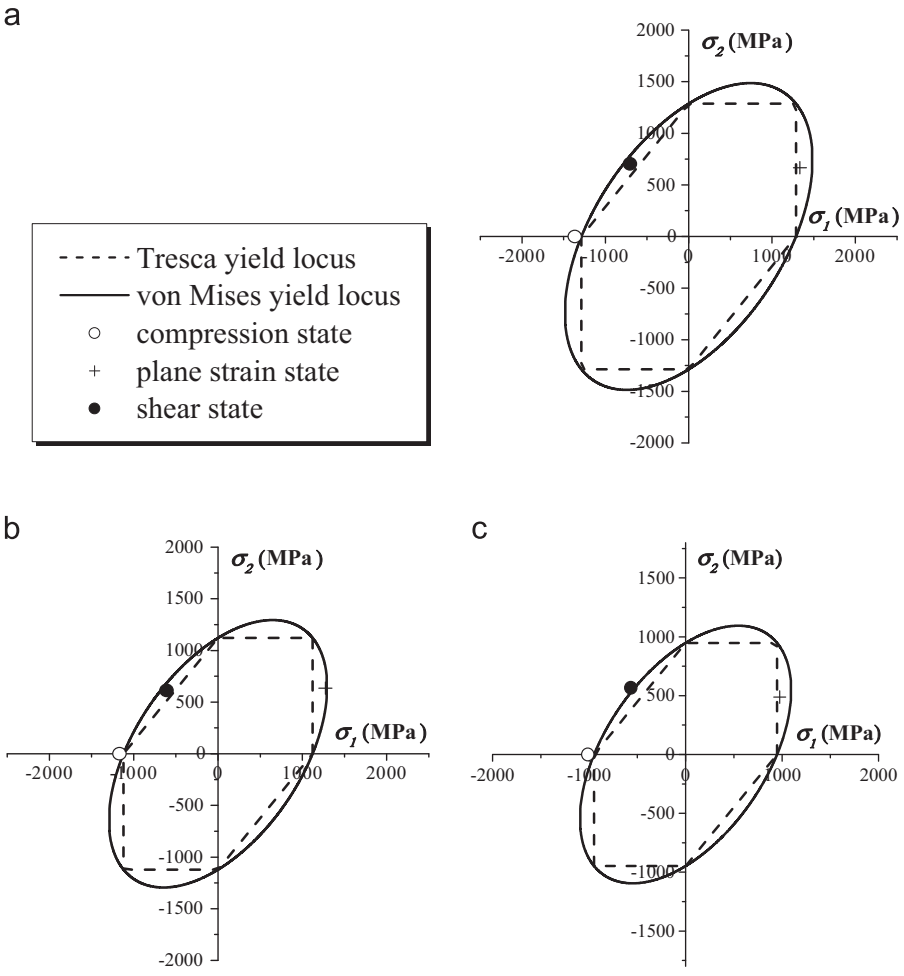

Fig. 12. Experimental points of the yield locus of Ti5553-1, Ti5553-3 and Ti–6Al–4V alloys compared to Tresca and von Mises: (a) Ti5553-1 alloy at $\dot{\varepsilon} = 5 \times 10^{-5}\ s^{-1}$; (b) Ti5553-3 alloy at $\dot{\varepsilon} = 5 \times 10^{-5}\ s^{-1}$; (c) Ti–6Al–4V alloy at $\dot{\varepsilon} = 1.2 \times 10^{-4}\ s^{-1}$.

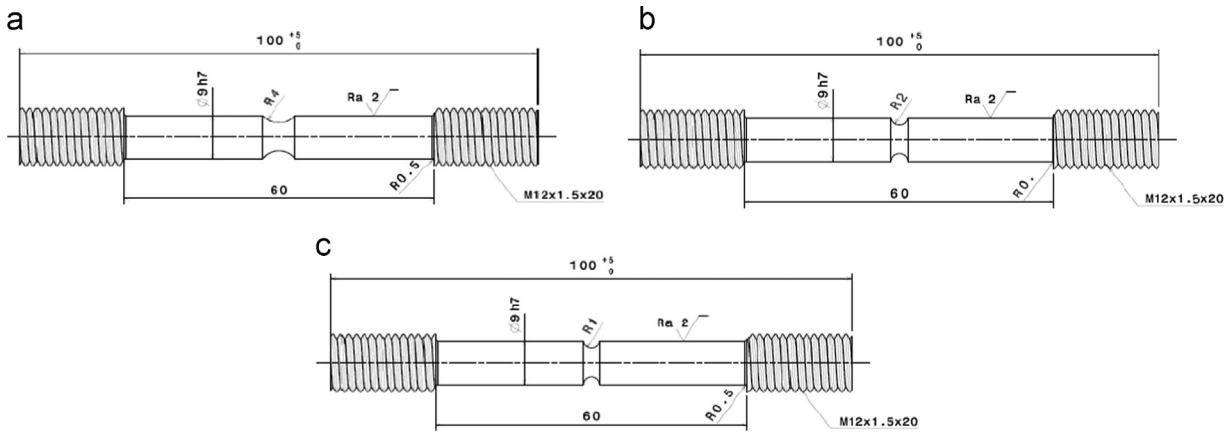

Fig. 13. Geometry of the simulated notched specimens (dimensions in mm): (a) $R_0=1$ mm, (b) $R_0=2$ mm, and (c) $R_0=4$ mm.

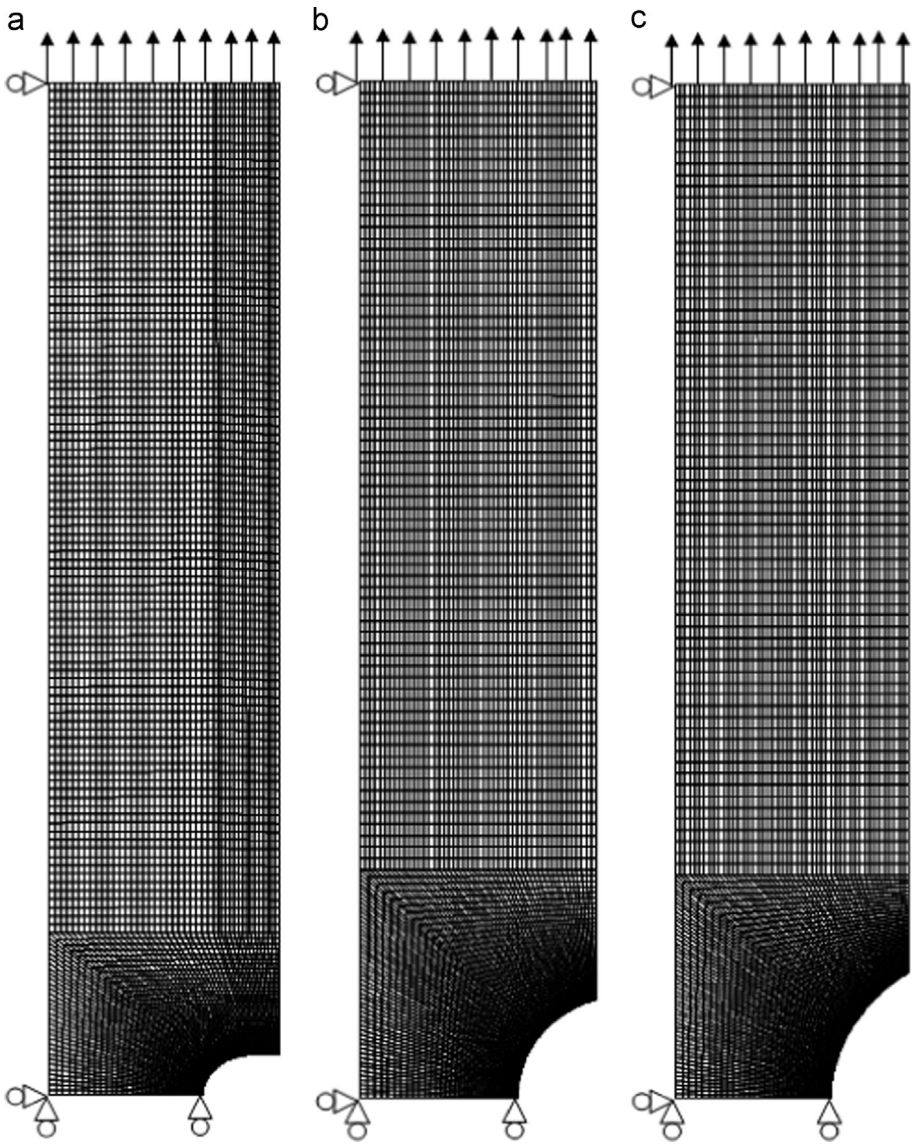

Fig. 14. Initial mesh and geometry of the notched specimens: (a) $R_0=1$ mm, (b) $R_0=2$ mm, and (c) $R_0=4$ mm.

As shown in Fig. 15, the comparison between the average tensile stress–average axial strain responses for the numerical simulations (presented in the figure with dashed lines) and the experiments (presented in the figure with solid lines), leads to almost perfect agreement between experiments and predictions for the three notch radii ($R_0=1$, 2 and 4 mm).

The average stress and the strain in the minimum cross-section are computed in the same way in the experiments and in FE

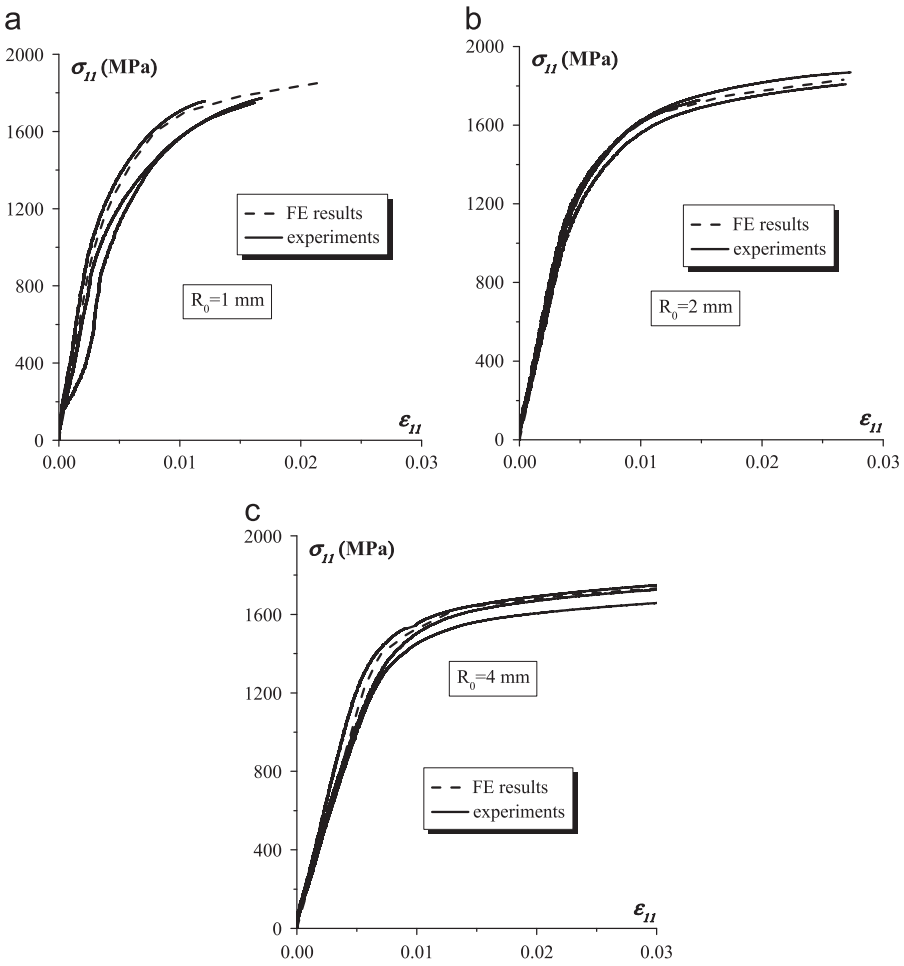

Fig. 15. Comparison between the experimental results and the numerical predictions: (a) R_0=1 mm, (b) R_0=2 mm, and (c) R_0=4 mm.

analysis, i.e. by using

$$\sigma_{11} = F/S; \quad \varepsilon_{11} = Ln(S_0/S) \tag{11}$$

where F is the tensile force, S_0 is the initial surface of the minimum cross section, and S is the current surface of the minimum cross section measured by extensometer.

5.2. Validation of the plane strain state and isotropy assumption

A finite element simulation of the plane strain test is performed using the FE code ABAQUS [44]. In these simulations, the elasto-viscoplastic parameters of the Ti–6Al–4V alloy at RT are used. The symmetry of the problem allows modeling one quarter of the specimen only. A vertical displacement up to 0.5 mm is imposed at the upper surface of the specimen. The displacement velocity is constant and equal to 0.005 mm/s as in the experimental tests. The nodes of the upper side of the specimen are constrained in the horizontal direction, to conform with the experimental conditions (Fig. 16).

Fig. 17 shows the distribution of the predicted strain components ε_{xx} (in the tensile direction) and ε_{yy} (in the width direction) at three particular deformation stages (corresponding to a vertical displacement equal to 0.1, 0.2 or 0.3 mm of the upper surface of the specimen). One can notice that the strain field is homogeneous on the deformation area except at the free edges. The magnitude of the strain component ε_{yy} is largely inferior to the magnitude of the strain component ε_{xx} and close to zero in the central zone, which confirms the plane strain assumption.

The plane strain state is further analyzed in Fig. 18. The predicted strain at the specimen free edges increases faster than the strain in the central zone (edge effect). Also, the minor strain evolution at the specimen center can be neglected when compared to the major strain measured in the same zone, justifying the plane strain condition. Moreover, a homogeneous strain field zone can be identified in the specimen central part, which decreases while the specimen is being plastically deformed.

Fig. 19 presents a comparison between the stress–strain curves extracted from plane strain tests. The following abbreviations are used in this figure:

- Exper: the stress–strain curves corresponding to the different experimental tests (three tests).
- FE-mic: the stress–strain response σ_{xx}–ε_{xx} of the central element of the specimen.
- NH: the stress–strain response σ_{xx}–ε_{xx} deduced from the Norton–Hoff model assuming perfect plane strain conditions; σ_{xx} and ε_{xx} are equal to $(2/\sqrt{3})\overline{\sigma}$ and $(\sqrt{3}/2)\overline{\varepsilon}$, respectively. The equivalent stress $\overline{\sigma}$ is related to the equivalent strain $\overline{\varepsilon}$ by the Norton–Hoff relationship (Eq. (4)).
- FE-mac: the stress σ_{xx} is equal to the tensile force F divided by S and the strain ε_{xx} is equal to Ln(S_0/S).

The following conclusions and observations can be drawn from Fig. 19:

- The curves FE-mic and NH are almost identical, which means that the central element is subjected to a plane strain state.

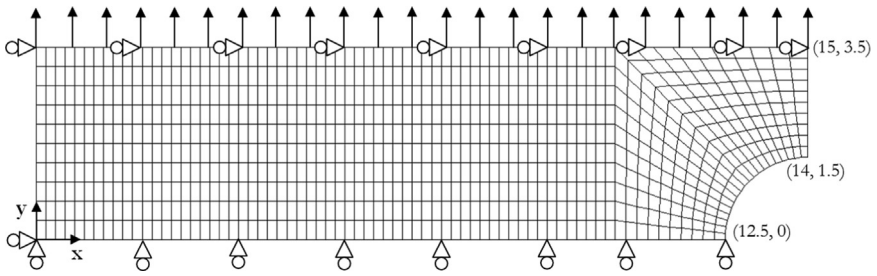

Fig. 16. Initial mesh and geometry of the plane strain specimen (mm).

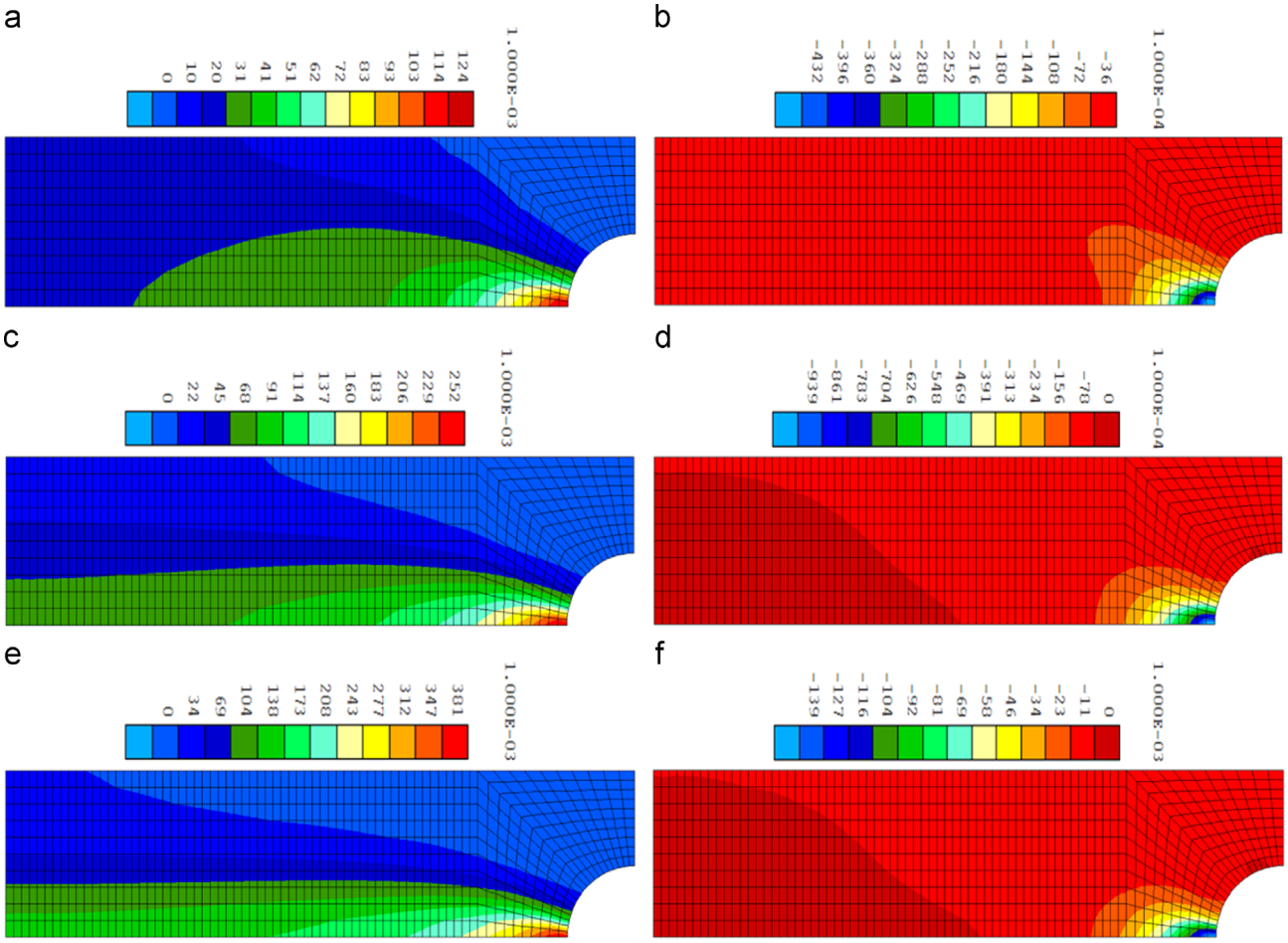

Fig. 17. Distribution of the predicted strain components in the plane strain specimen. (a) ε_{xx} at u=0.1 mm, (b) ε_{yy} at u=0.1 mm, (c) ε_{xx} at u=0.2 mm, (d) ε_{yy} at u=0.2 mm, (e) ε_{xx} at u=0.3 mm and (f) ε_{yy} at u=0.3 mm.

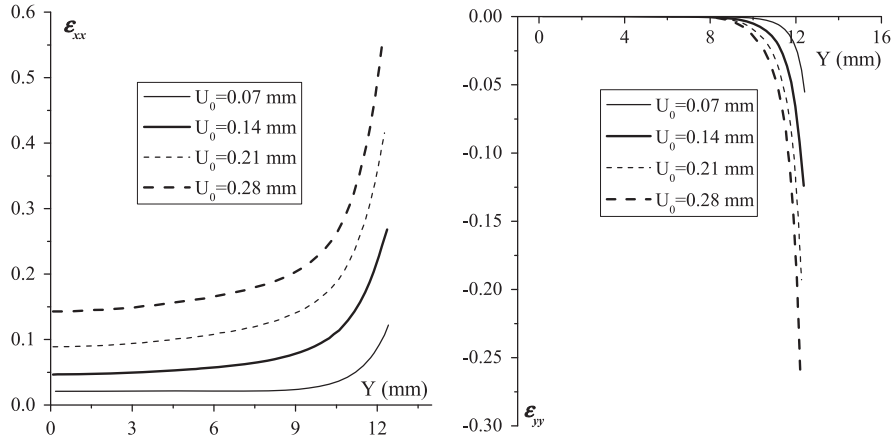

Fig. 18. Validation of the plane strain assumption: local level.

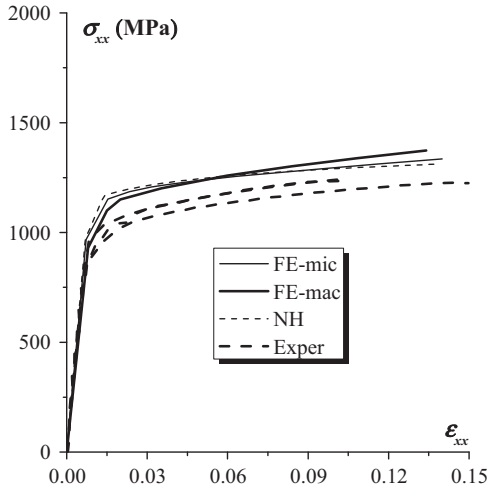

Fig. 19. Correlation between experimental and numerical predictions: global level.

- FE-mic (as a consequence NH) curve and FE-mac curve are identical at the beginning of the loading and the difference between the two curves increases with deformation. This is due to the development of heterogeneous deformations at the boundary of the specimens. This heterogeneous deformation zone is very weak and very localized at the beginning of the loading and gradually grows as previously demonstrated in Figs. 18 and 19.
- The experimental curves are different from the theoretical curve NH and from the numerical curves FE-mic and FE-mac. This difference is due to the weak experimental anisotropy which is neglected in the model. This result can easily be correlated to the shape of the yield locus shown in Fig. 12.

6. Conclusions

A wide mechanical testing campaign has been performed to characterize the elastoviscoplastic behavior of two microstructures of the Ti5553 alloy and of a reference Ti–6Al–4V alloy. The isotropic elastic parameters and the Norton–Hoff viscoplastic parameters were identified at room temperature and at 150 °C from uniaxial tensile tests. On the basis of the experimental data available, it can be concluded that the tensile strength of the Ti5553-1 and Ti5553-3 microstructures is larger than that of the Ti–6Al–4V by about 40% and 20%, respectively. The Ti5553 alloy constitutes thus a promising material for advanced structural applications compared to the traditional Ti–6Al–4V alloy. The elastic and plastic anisotropy was analyzed based on a variety of mechanical tests. The anisotropy is weak and can be neglected in structural analysis or forming applications without significantly affecting the accuracy of the numerical predictions. This conclusion will simplify the work of designers in view of the increased difficulty to simulate the deformation of components with anisotropic laws.

Acknowledgments

The authors thank the Walloon Region (Titaero Project), the Belgian Scientific Research Fund FNRS, Belgium which finances A. M.H. and the Interuniversity Attraction Poles Program, Belgian Science Policy P7/21 INTEMATE, for their financial support.

References

[1] R.R. Boyer, R.D. Briggs, J. Mater. Eng. Perform. 14 (2005) 681–685.
[2] P.-J. Arrazola, A. Garay, L.-M. Iriarte, M. Armendia, S. Marya, F. Le Maitre, J. Mater. Process. Technol. 209 (2009) 2223–2230.
[3] J.D. Cotton, R.R. Boyer, R.D. Briggs, R.G. Baggerly, C.A. Meyer, M.D. Carter, W. Wood, G. Tewksbury, V. Li, X. Yao, in: M. Niinomi, S. Akiyama, M. Hagiwara, M. Ikeda, K. Maruyama (Eds.), Titanium 2007: Science and Technology, 1, The Japanese Institute of Metals, 2007, pp. 471–479.
[4] G. Lütjering, J.C. Williams, Titanium, 2nd ed., Springer, Berlin, Germany, ISBN 978-3-540-71397-5, 2007.
[5] M. Jackson, N.G. Jones, D. Dye, R.J. Dashwood, Mater. Sci. Eng. A 501 (2009) 248–254.
[6] P. Moureaux, S. Moto Mpong, M. Remy, C. Bouffioux, J. Lecomte-Beckers, A.M. Habraken, J. Phys. IV—Proc. 12 (2002) 361–368.
[7] R. Boyer, G. Welsch, E.W. Collings, Materials Properties Handbook, Titanium Alloys, ASM International, Metal Park, OH (1994) 483.
[8] G. Lutjering, J.C. Williams, Titanium, Springer-Verlag, Berlin, 2003.
[9] S.L. Semiatin, V. Seetharaman, I. Weiss, Mater. Sci. Eng. A 243 (1998) 1–24.
[10] R. Ding, Z.X. Guo, A. Wilson, Mater. Sci. Eng.: A 327 (2002) 233–245.
[11] Y. Millet, Journées Technologiques Titane 2007, The French Titanium Association, Nantes, France.
[12] J.J. Brioist, Ph.D. thesis, Ecole Nationale Supérieure des Mines de Paris, 1995.
[14] B. Baufeld, O. van der Biest, Sci. Technol. Adv. Mater. 10 (2009) 1468–1469.
[15] A. Kierzkowska, M. Malinowski, E. Krasicka-Cydzik, J. Achiev. Mater. Manuf. Eng. 18 (2006) 139–142.
[16] Q. Hong, G.-J. Yang, Y.-Q. Zhao, Y.-L. Qi, P. Guo, Trans. Nonferrous Met. Soc. China 17 (2007) 218–222.
[17] M. Vanderhasten, Ph.D. thesis, KUL, Belgium, 2007.
[18] G. Bruno, B.D. Dunn, Meas. Sci. Technol. 8 (1997) 1244–1249.
[19] D.T. Queheillalt, B.W. Choi, D.S. Schwartz, H.N.G. Wadley, Metall. Mater. Trans. A: Phys. Metall. Mater. Sci. 31 (2000) 261–273.
[20] T.A. Venkatesh, B.P. Conner, C.S. Lee, A.E. Giannakopoulis, T.C. Lindley, S. Suresh, Metall. Mater. Trans. A 32 (2001) 1131.
[21] A. Modgil, Master thesis, University of Florida, 2003.
[22] M. Vanderhasten, L. Rabet, B. Verlinden, Mater. Des. 29 (2008) 1090–1098.
[23] F.H. Norton, Mc Grow-Hill, The Creep of Steel at High Temperature, New-York, 1929, p. 219.
[24] N.J. Hoff, Q. Appl. Mech. 12 (1954) 49–55.
[26] J.A. Nelder, R. Mead, Comput. J. 7 (1965) 308–313.
[27] E.O. Hall, Proc. Phys. Soc. B 64 (1951) 747–753.
[28] S.L. Semiatin, T.R. Bieler, Acta Mater. 49 (2001) 3565–3573.
[29] B.D. Venkatesh, D.L. Chen, S.D. Bhole, Mater. Sci. Eng. A 506 (2009) 117–124.
[30] Y. Yulan, W. Weiqi, L. Fengli, L. Weiqing, Z. Yongqiang, Mater. Sci. Forum 618–619 (2009) 169–172.
[31] N.J. Petch, J. Iron Steel Inst. 174 (1953) 25–28.
[32] M. Delincé, Y. Bréchet, J.D. Embury, M.G.D. Geers, P.J. Jacques, T. Pardoen, Acta Mater. 55 (2007) 2337–2350.
[33] H. Pijlman, Ph.D., University of Twente, Netherlands, 2002.
[34] P. Flores, P. Moureaux, A.M. Habraken, Adv. Exp. Mech. IV (2005) 91–97.
[35] P. Flores, E. Rondia, A.M. Habraken, Int. J. Form. Process. (2005) 117–137.
[36] P. Flores, V. Tuninetti, G. Gilles, P. Gonry, L. Duchêne, A.M. Habraken, J. Mater. Process. Technol. 210 (2010) 1772–1779.
[37] G. Gilles, V. Tuninetti, M. Ben Bettaieb, O. Cazacu, A.M. Habraken, L. Duchêne., Numisheet, 2011.
[38] P. Flores, Ph.D. thesis, University of Liège, Belgium, 2005.
[39] G. Gilles, W. Hammami, V. Libertiaux, O. Cazacu, J.H. Yoon, T. Kuwabara, A.M. Habraken, L. Duchêne, Int. J. Solids Struct. 48 (2011) 1277–1289.
[40] O. Cazacu, B. Plunkett, F. Barlat, Int. J. Plast. 22 (2006) 1171–1194.
[41] B. Plunkett, O. Cazacu, F. Barlat, Int. J. Plast. 24 (2008) 847–866.
[42] M.E. Nixon, O. Cazacu, R.A. Lebensohn, Int. J. Plast. 26 (2010) 516–532.
[43] Y.Y. Zhu, S. Cescotto, A.-M. Habraken, J. Mater. Process. Technol. 32 (1992) 197–204.
[44] ABAQUS 6.9, Simulia, Inc., Providence, RI, USA, 2009.